remote sensing

MDPI

Article

Magnetic Anomaly Characteristics and Magnetic Basement Structure in Earthquake-Affected Changning Area of Southern Sichuan Basin, China: A New Perspective from Land-Based Stations

Chao Dong *, Bin Chen and Can Wang

Institute of Geophysics, Chinese Earthquake Administration, Beijing 100080, China
* Correspondence: dongchao@cea-igp.ac.cn

Abstract: The Changning area is located in the southern Sichuan basin and the western Yangtze Plate and is the most abundant shale gas exploration area in China. In recent years, Changning has experienced frequent earthquakes with moderate magnitudes, attracting extensive interest. To investigate the magnetic characteristics in Changning, 952 land-based stations were employed to establish a magnetic anomaly model with a resolution of 2 km, and the subsurface magnetic basement structure was obtained by an iterative algorithm in the Fourier domain. The magnetic anomaly model shows significant distinctions between the northern salt mine area and the southern shale gas area. The magnetic basement includes the crystalline basement and the Sinian sedimentary rock metamorphic basement, which has strong magnetism. The large intracratonic rift that developed in the Sinian–Early Cambrian plays an important role in the evolution of Changning, which also impacts magnetic anomalies and the magnetic basement structure. Finally, by comparing the seismic wave velocity ratio structure, the deeper magnetic basement that corresponds to the higher seismic wave velocity ratio can be explained. This article implies that magnetic anomalies and magnetic basement depth have a certain correlation with earthquakes in Changning, and it provides a geodynamic reference for Changning and the southern Sichuan basin.

Keywords: magnetic anomalies; land-based stations; magnetic basement; Changning; earthquakes

Citation: Dong, C.; Chen, B.; Wang, C. Magnetic Anomaly Characteristics and Magnetic Basement Structure in Earthquake-Affected Changning Area of Southern Sichuan Basin, China: A New Perspective from Land-Based Stations. *Remote Sens.* **2023**, *15*, 23. https://doi.org/10.3390/rs15010023

Academic Editor: Angelo De Santis

Received: 24 October 2022
Revised: 16 December 2022
Accepted: 16 December 2022
Published: 21 December 2022

1. Introduction

The Sichuan basin is in the Yangtze terrane of the South China craton and lies on the eastern edge of the north–south seismic zone in China, which became a stabilized cratonic rigid block in the late Neoproterozoic [1–3]. The sedimentary layers inside the Sichuan basin are less deformed, but the crust surrounding the basin underwent intense deformation from the Mesozoic to the Cenozoic, including the Dabashan thrust fault belt and the Longmenshan thrust fault belt, which are still active and cause earthquakes [1,4].

In addition to the Longmenshan fault, another high-seismicity area in the Sichuan basin is the Changning area, which is located at the southern edge of the Sichuan basin, and at the junction between the Tibetan plateau and the Yangtze terrane (Figure 1). At the same time, Changning is one of the areas with the highest potential for shale gas and salt well development in China. Shale gas hydraulic fracturing and salt well water reinjection have induced a relatively high frequency of moderate earthquakes in the Changning area [5–7] and have attracted extensive interest in recent years.

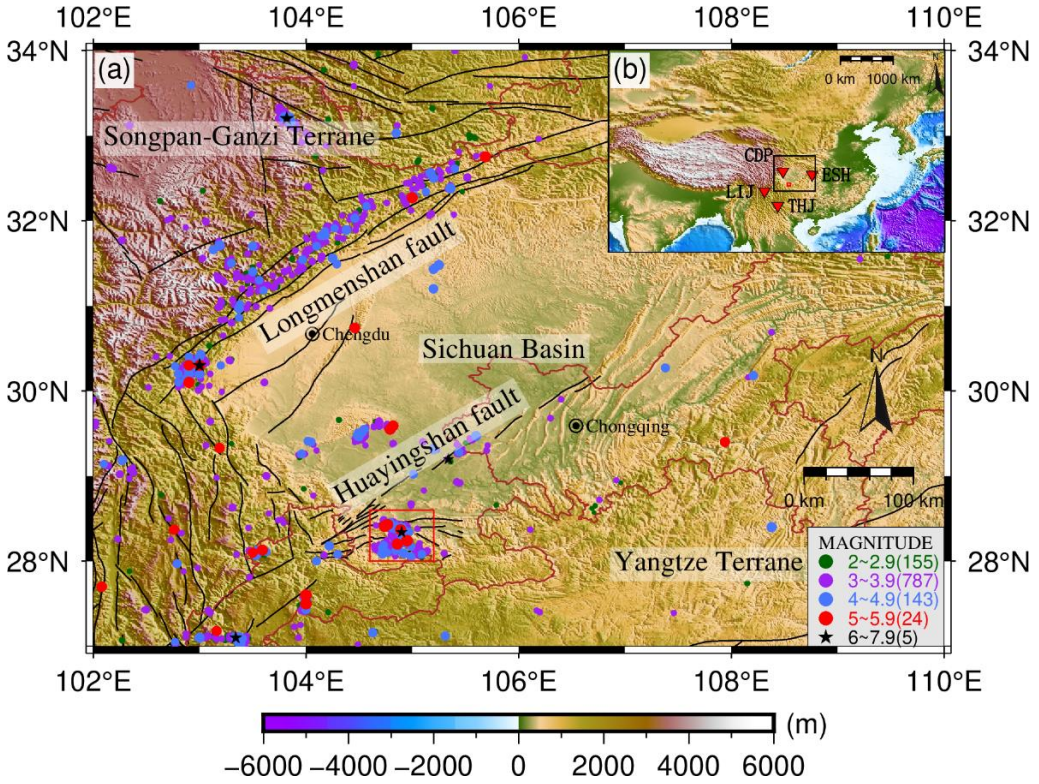

Figure 1. Distribution characteristics of earthquakes in the Sichuan basin and surrounding areas. The red rectangle is the study area. The main faults are marked with black lines [8]. The brown lines are the provincial boundaries. The magnitude numbers in the Sichuan basin are shown in the lower right corner. Different colors represent different earthquake magnitudes. The location of the Sichuan basin is shown in a black rectangle, and the four red triangles are the geomagnetic observatories employed for diurnal variation reduction in Section 3.1, in Figure 1b. CDP: Chengdu geomagnetic observatory. ESH: Enshi geomagnetic observatory. LIJ: Lijiang geomagnetic observatory. THJ: Tonghai geomagnetic observatory. The earthquake catalog is from 2012.03 to 2022.03.

Industrial activities, such as unconventional oil and gas development, have enhanced geothermal systems, CO_2 and waste brine deep infusion, whereby high-pressure fluids are injected into the subsurface, which causes increased deep fluid pressure, rock temperature changes, and stratigraphic deformation, and potentially leads to the activation of existing faults, which induces earthquakes [9]. The main reason for the increasing prevalence of earthquakes in Oklahoma, USA, in recent years is waste brine reinjection [10]. The earthquakes in Alberta, Canada, are caused by hydraulic fracturing [11]. In addition, earthquakes in Lancashire, UK, have been induced by the hydraulic fracturing of the Preese Hall borehole, and earthquakes in the Groningen gas field have been induced by industrial water injection in the Netherlands [9,12].

As shown in Figure 2, the Changning area is divided into two main earthquake clusters, indicated by ellipses [6]. The green ellipse earthquake cluster is located within the Changning anticline, which is underlain by salt mine N2 [13]. Many studies have shown that salt well water reinjection induces earthquake activities [6,14]. The blue ellipse earthquake cluster is located around the Jianwu syncline, primarily between the Luochang syncline and the Jianwu syncline. This is a shale gas area; N201 and N203 are shale gas exploration wells [13], and many studies have shown that earthquakes are induced by shale gas hydraulic fracturing [5,14–16]. The complex outcropped faults with different complex geometry scales, and the deficiency of surface ruptures in these earthquakes, increase the difficulty of studying earthquake mechanisms and seismogenic faults [13].

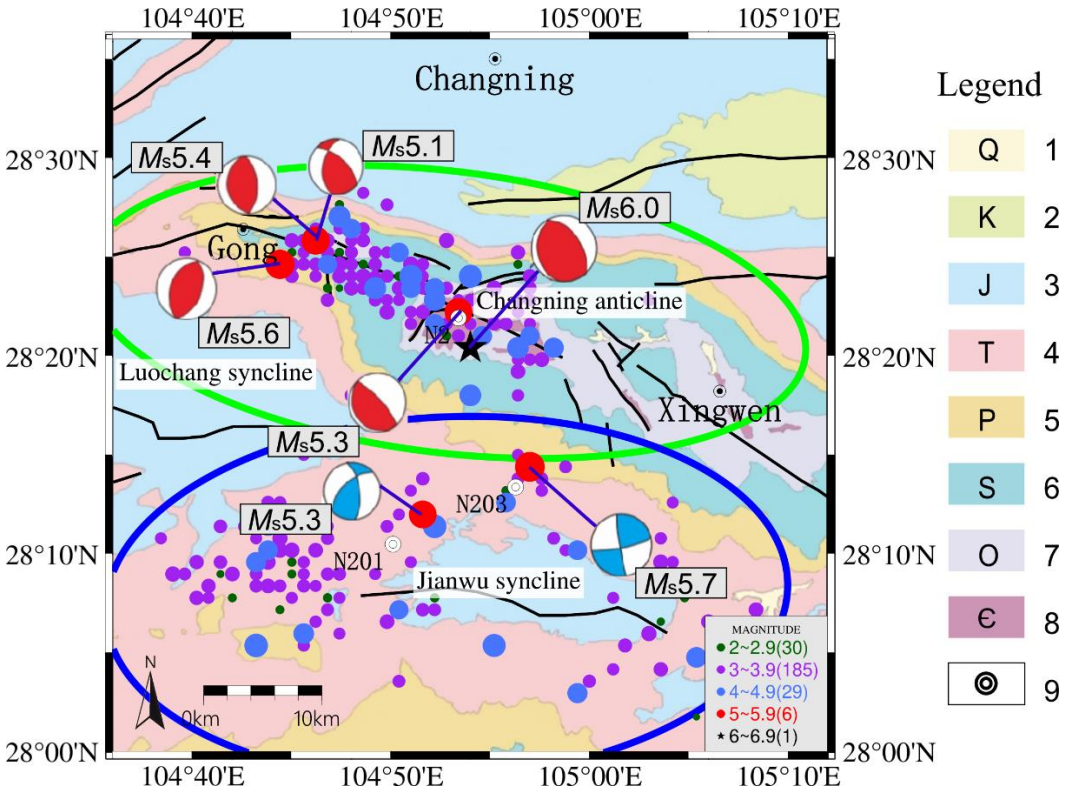

Figure 2. Distribution characteristics of earthquakes and geological settings (modified from [13]) in the Changning area. The focal mechanism plots indicate the focal mechanism solutions of moderate earthquakes; red is in the Changning anticline, and blue is in the Jianwu syncline [13]. The two ellipses are earthquake clusters [6]. The black lines represent the fault line in the Changning area, including tectonic lines and surveyed faults [5,17]. The magnitude numbers are shown in the lower right corner. Different colors represent different earthquake magnitudes. The earthquake catalog is from 2012.03 to 2022.03. Legend: 1, Cenozoic; 2, Cretaceous; 3, Jurassic; 4, Triassic; 5, Permian; 6, Silurian; 7, Ordovician; 8, Cambrian; 9, drilling well.

Many instruments are used to measure the Earth's magnetic fields, such as satellite, aeromagnetic, marine and land-based observatories, as well as land-based stations, which can show the position and strength of Earth's invisible magnetic field [18–20]. Research has shown that earthquake occurrences are accompanied by changes in geological structure, rock properties, stress states and temperature, which can cause magnetic anomalies [21–26]. Other studies have shown that seismic activity is associated with the curie depth, which is the bottom interface of the magnetic basement, and is estimated via the spectral analysis of magnetic data [27,28].

More recent investigations have shown that positive magnetic anomalies in the Sichuan basin spread widely in the NE–SW direction, interspersed with negative magnetic anomalies, but the resolution was not high enough and could not reflect local magnetic anomalies in the Changing area [3,18,29,30].

The total magnetic field data used in this article are derived from land-based stations. Compared with satellite data and aeromagnetic data, the advantages of land-based station data are that they accurately reflect the geomagnetic field's strength at the measurement station, with higher resolution. Magnetic anomaly datasets are used to characterize the subsurface in order to yield a more accurate image of the magmatic and deformational evolution of areas hidden beneath sedimentary cover [31]. The strongly magnetized rocks in the Precambrian basement are covered by non-magnetic sedimentary layers from the Neoproterozoic to Cenozoic in the Sichuan basin, and the magnetic source is not exposed on the surface [29]. Dong et al. and Gao et al. stated that the non-magnetic sedimentary layers

were at 4 to 10 km deep [1,2], but Li et al. stated they were at 5 to 12 km [32]. Many methods have been applied in magnetic crystalline basement topography mapping, including the iterative inversion method [33–35], the Euler deconvolution algorithm [36–38], spectral method inversion [39–42], and so on. Among them, Parker's inversion method [33] has been widely used because of its ability to effectively distinguish lateral variations in the subsurface's physical properties, and its fast calculation speed [34,35].

This article is structured as follows: The geological setting is introduced in the second section. In the third section, a local magnetic anomaly model is established in Changning, and a rapid iterative algorithm in the Fourier domain is applied to estimate the subsurface magnetic basement topography. In the fourth section, we analyze the seismic activity and geological structure in Changning from the perspectives of the magnetic anomaly characteristics and the magnetic basement structure. Finally, the summary and conclusions are given in the last section.

2. Geological Setting

The study area is located at the junction of the Sichuan, Yunnan and Guizhou provinces. Its western area is affected by the remote extrusion stress of the Longmenshan fault, the northern area is limited by the Sichuan basin and Huayingshan fault, and the southern and eastern areas are superimposed via the simultaneous compression and uplift caused by tectonic transformation, which together form the present tectonic framework [1,2,43].

As shown in Figure 2, the Changning anticline is northwest–west trending, curved, dips to the west at the western end, and extends about 50 km, widely in the east and narrowly in the west [5,14]. The characteristics of the Changning anticline axis show a steep northeast flank, and a gentle southwest flank, which is connected to the Luochang syncline—a wide and flat syncline [5]. A series of thrust faults emerged at the core of the Changning anticline, which outcrop the Cambrian, Ordovician, Silurian, Permian, Triassic and Jurassic deposits in the periphery [44–46]. The strata are well developed in the Changning area, with a strongly magnetized Pre-Sinian crystalline basement, covered with a weakly magnetized Mesozoic and Paleozoic sedimentary thickness of more than 9 km [3,13,43]. The Jianwu syncline is in the south of the Changning anticline, trending in the WE direction. Neither flanks are steep, and the strata integrity is good; the Middle Jurassic Shaximiao Formation is outcropped at the core of the Jianwu syncline [43,46].

In the southern Sichuan basin, the lower Silurian Longmaxi Formation and upper Ordovician Wufeng Formation are the main shale gas reservoirs. The Sinian Dengying Formation comprises the target layer for salt mining [5,13,44].

3. Materials and Methods

3.1. Magnetic Data and Processing

In total, 952 land-based geomagnetic stations, with a spacing of about 2 km, were deployed in the Changning area from November 2019 to December 2019, as indicated by the solid dots in Figure 3a. GSM-19T proton precession magnetometers are employed in the magnetic survey method. Each station is composed of a main sensor post and an auxiliary sensor post, with a distance of no less than 20 m between them. To ensure the reliability and accuracy of the measurements, each station was carefully placed to avoid manmade electromagnetic interference. Three sets of observations were taken at each station to minimize the measurement error, and gradient measurement was utilized to confirm local homogeneity; the horizontal gradient and vertical gradient obtained in the survey were less than 3 and 5 nT/m, respectively.

The Earth's magnetic field is mainly composed of the main magnetic field, the lithospheric magnetic field and the exogenous magnetic field [18]. The main magnetic field is understood to be generated by the flow of liquid plasma in the outer core, as described by the geodynamo theory [47,48]. The exogenous field mainly comprises the magnetic field generated by the Earth's external environment, such as the magnetosphere magnetic field and the ionosphere magnetic field. To obtain magnetic anomaly data, it is necessary to

eliminate the influence of magnetic fields from other sources and process the observed data uniformly, resorting to the use of properly selected observatories [18,49].

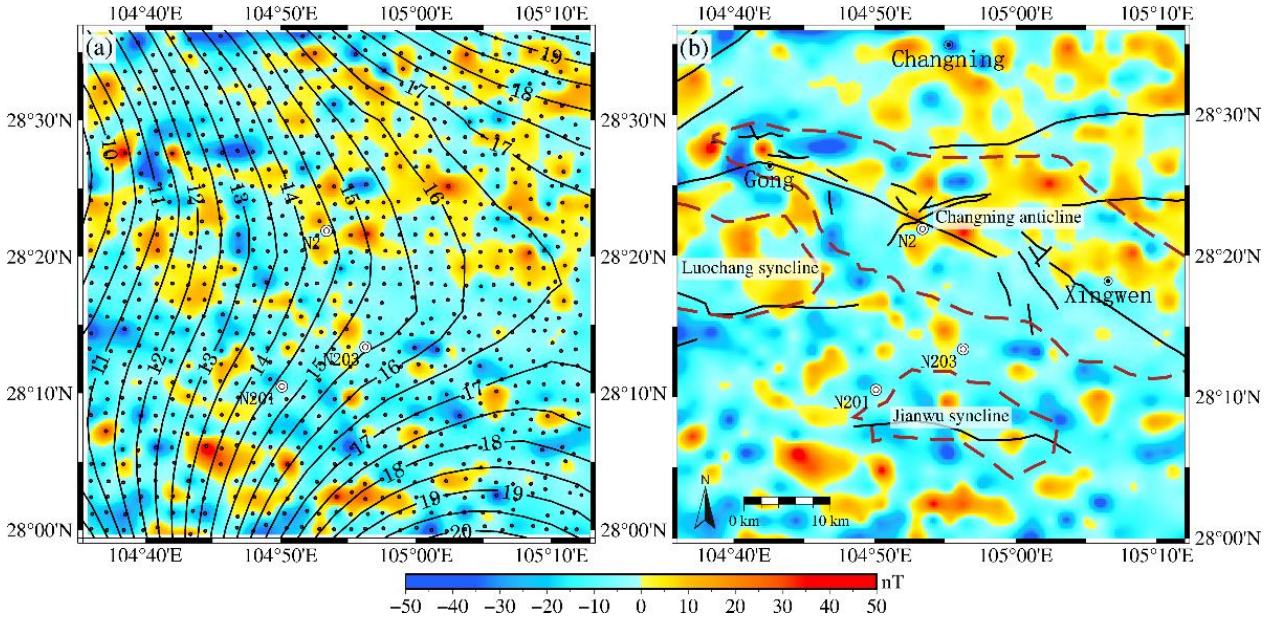

Figure 3. Magnetic anomalies in the Changning area. Black solid contour lines indicate magnetic anomalies given by EMAG2v3 in (**a**). In (**b**), the black lines represent the fault line in the Changning area, including tectonic lines and surveyed faults [5,17]. The brown lines are the fold structure in the study area.

Firstly, in order to eliminate the influence of the exogenous magnetic field and reduce the errors caused by the selected observatories, the Chengdu, Enshi, Lijiang and Tonghai geomagnetic observatories (Figure 1b), which are closest to the study area in each of the four cardinal directions, were selected to ensure diurnal variation reduction. The four diurnal variation results of each observatory were weighted by the inverse ratio of observatory distance with respect to the station, and the calculation formula is as follows:

$$F_P^0 = \frac{1}{M \times \sum_{n=1}^{N} \frac{1}{r_n}} \times \sum_{n=1}^{N} \sum_{m=1}^{M} \frac{F(t_m) - [F_n(t_m) - F_n(t_0)]}{r_n} \quad (1)$$

in which $F^0{}_P$ is the result for station P after the elimination of the external field by daily variation correction at t_0. In this article, t_0 refers to 16:00~19:00 on 18 November 2019, which was the closest magnetically quiet day to the period of field measurement. N is the number of geomagnetic observatories, M is the measuring number, t_m is the mth measuring time, $F(t_m)$ is the measured value at t_m, $F_n(t_m)$ is the measured value of the nth observatory at t_m, $F_n(t_0)$ is the average value of the nth observatory at t_0, and r_n is the distance in km from the measuring station to the nth observatory.

Secondly, the main geomagnetic field was removed to obtain the spatial distribution of the lithospheric magnetic field. The calculation formula is as follows:

$$F_P^a = F_P^0 - F_P^n \quad (2)$$

in which F_P^a is the lithospheric magnetic field value after being stripped of the main geomagnetic field at station P, and F_P^n is the main geomagnetic field value at station P. The internal origin main magnetic field, as given by the International Geomagnetic Reference Field (IGRF-13), was subtracted from the Earth's magnetic field [50]. Magnetic anomalies in the Changning area are shown in Figure 3.

3.2. Reduction to the Pole

Reduction to the pole (RTP) was applied to the total field magnetic anomaly data to reduce the effect of the geomagnetic field and the magnetization of the source, which were not vertical. RTP uses the Fast Fourier Transform (FFT) in the frequency domain; the transform filter is

$$RTP(k_x, k_y) = \frac{|k|^2}{a_1 k_x^2 + a_2 k_y^2 + a_3 k_x k_y + i|k|(b_1 k_x + b_2 k_y)}, \ |k| \neq 0, \tag{3}$$

in which

$$\begin{aligned} |k| &= \sqrt{k_x^2 + k_y^2}, \\ a_1 &= m_z f_z - m_x f_x, \\ a_2 &= m_z f_z - m_y f_y, \\ a_3 &= -m_y f_x - m_x f_y, \\ b_1 &= m_x f_z + m_z f_x, \\ b_2 &= m_y f_z + m_z f_y, \end{aligned}$$

where k_x and k_y are the wave numbers in the x and y directions, and their Euclidean norm $|k|$ is in 2 π/km; $m = (m_x, m_y, m_z)$ is the unit vector of the total magnetization of the source, and $f = (f_x, f_y, f_z)$ is the unit vector of the geomagnetic field [35]. The Chengdu, Enshi, Lijiang and Tonghai observatories (Figure 1b) were used to fit the inclination and declination of the ambient field. In our study area, the inclination and declination of the magnetization were 45.3° and −2.36°, respectively, and the magnetization direction was assumed to be parallel to the direction of the ambient field [3]. The magnetic anomalies after RTP in the Changning area are shown in Figure 4b.

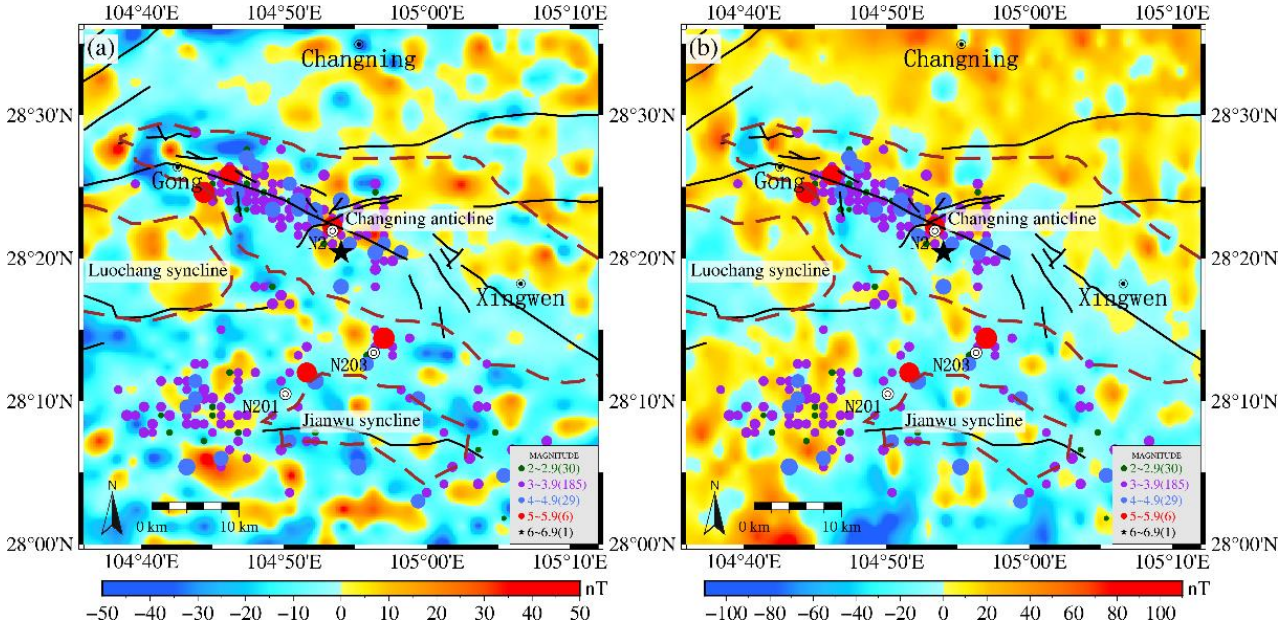

Figure 4. Distribution characteristics of earthquakes in the Changning area; (**a**) shows the contour map of the magnetic anomalies, while (**b**) shows the same contour map after RTP. Different colors represent different earthquake magnitudes. The earthquake catalog is from March 2012 to March 2022.

3.3. Inversion theory

The method used to estimate the magnetic basement relief of the Changning area was based on an iterative algorithm with the Fourier transforms of the geomagnetic data and the interface topography [33,35]. The method involved the estimation of the magnetic slab depth derived from magnetic anomaly data. The MagB_inv code was used to calculate the

magnetic basement depth [34]. The 3D Fourier transforms of the magnetic anomaly data ΔT can be described as [33]

$$F[\Delta T] = 2\pi M \Theta_f \Theta_m C_m e^{-|k|Z_0} \sum_{n=1}^{\infty} \frac{(-|k|)^n}{n!} F[h^n], \quad (4)$$

in which F denotes Fourier transformation, M is the magnetization contrast, θ_m and θ_f are the directional factors for the magnetization direction and geomagnetic field direction, respectively, C_m is the magnetic permeability, k is the wave number (which is defined in Equation (3)), Z_0 is the average interface depth of the magnetic slab, h is the magnetization layer depth, and n is a natural number of h.

The depth of the undulate interface h was calculated from the magnetic anomaly data by means of an iterative inversion procedure, given by [34]

$$F[h] = \lim_{t\to\infty} F[h] = -\frac{F[\Delta T]}{2\pi M|k|\Theta_f \Theta_m C_m e^{-|k|Z_0}} - \sum_{n=2}^{t} \frac{(-|k|)^{n-1}}{n!} F[h^n], \quad (5)$$

in which t stands for iteration steps. This initial value of h was used to evaluate the right-hand side of Equation (5). The initial estimated value of h was 6 km [13,32,43,46,51,52] and the magnetization contrast was 2 A/m [53,54] in this paper. Following the iteration, this quantity was then used in Equation (5) to refine the topography interface. The difference between two successive h values can be quantified by a root mean square (RMS) error, defined by [34]

$$RMS = \sqrt{\frac{\sum_{i=1}^{M}\sum_{j=1}^{N}\left(h_{i,j}^{t+1} - h_{i,j}^{t}\right)^2}{M \times N}}, \quad (6)$$

where M and N are the numbers of grid nodes along the y-axis (north) and x-axis (east), respectively. The RMS process was continued until a specified number of iterations had been completed or the RMS error of two sequential iterations in Equation (5) satisfied a presumed accuracy; alternatively, it stopped the instant the RMS error magnitude exceeded its previous value.

A high-cut filter was used to ensure the convergence of the series in the above equation and to avoid its instability at high frequencies. This filter is defined by [34,55]

$$B(k) = \left\{ \begin{array}{c} 1 \\ 1/2\left[1 + cos\left(\frac{k-2\pi WH}{2(SH-WH)}\right)\right] \\ 0 \end{array} \right\}, \; WH \leq \begin{array}{c} |k/2\pi| < WH \\ |k/2\pi| \leq SH \\ |k/2\pi| > SH \end{array}, \quad (7)$$

in which WH and SH are the roll-off frequency parameters of the filter. The proper choice of SH/WH can be inferred by analyzing the data of the power spectrum [34]. In this article, the values of WH and SH are 0.1 and 0.2, respectively. We estimated the magnetic basement relief map of the Changning area, and this is shown in Section 4.2.

4. Results and Discussion

4.1. Characteristics of Magnetic Anomaly

The total intensities of lithospheric magnetic anomalies were obtained in the range of −400~200 nT by processing after Section 3.1. High and low magnetic high data were excluded, and more than 95% of the measured data were retained. In this article, the final magnetic anomalies were around ±50 nT. In Figure 3a, the magnetic anomalies of EMAG2v3 (Earth Magnetic Anomaly Grid, 2-arc-minute resolution) are between 9 and 20 nT [18], and the aeromagnetic data show magnetic anomalies of about 0–20 nT in the Changning area [29]. In general, satellite, aeromagnetic and magnetic anomaly models cannot describe local magnetic anomalies in detail in the Changning area.

In Figure 3b, the total intensity of positive and negative magnetic anomalies in the study area are distributed alternately; they are complex, and mainly distributed in clusters, points and bands. Negative magnetic anomalies are distributed in most of Changning, and positive magnetic anomalies are mainly concentrated in the northeast and are scattered in the west and south. Magnetic anomalies along the NW–SE anticline axis direction (consistent with the anticline strike) are positive in the north and negative in the south in the Changning anticline, which is also in agreement with the fault. The western part of the Changning anticline is the most complex area, with alternating highly positive and negative magnetic anomalies. In the middle of the anticline, the faults are broken and complex, corresponding to negative magnetic anomalies inserted into positive magnetic anomalies. The Luochang syncline contains mostly positive magnetic anomalies, and the Jianwu syncline contains mostly negative magnetic anomalies, mixed with scattered positive magnetic anomalies.

Figure 4 shows the relationship between the distribution characteristics of earthquakes and magnetic anomalies. In Figure 4a, we see that earthquakes are mostly distributed in the magnetic anomaly zero-line area; in particular, seven earthquakes were observed above *M*s5.0 all within 2 km of the magnetic anomaly zero contour line (two earthquakes in the southeast of Gong were close to each other and cannot be distinguished in the figure). In the Changning anticline, earthquakes are concentrated in the northwest along the fault, and there were no earthquakes in the eastern region. There were no earthquakes in the Luochang syncline either. Around the Jianwu syncline, there is little correlation between earthquakes and magnetic anomalies. The earthquakes are mainly distributed in the west of the Jianwu syncline. The magnetic anomaly characteristics are significantly distinct between the north and south of the study area. The continuity of magnetic anomalies in the Changning anticline is better, while the Jianwu syncline's magnetic anomalies are distributed in a relatively scattered manner, with a point-like distribution. The distribution of earthquakes in these two areas also corresponds to the magnetic anomaly characteristics. In the northern part of the study area, earthquakes are concentrated in the Changning anticline, while in the southern area, the earthquakes are scattered.

In Figure 4b, the magnetic anomalies better reflect the magnetic sources after RTP. The negative magnetic anomalies are mostly concentrated in the south and southeast, and the positive magnetic anomalies are mainly concentrated in the north, northeast and west. Magnetic anomalies are more pronounced, with positive magnetic anomalies in the north and negative magnetic anomalies in the south along the NW–SE orientation of the Changning anticline. The magnetic anomalies are obviously negative in the east and positive in the west in the Luochang syncline, and the area of negative magnetic anomalies becomes larger in the Jianwu syncline. From the perspective of earthquake distribution, in the Changning anticline, earthquakes are concentrated in the northwestern region along the fault, which is more obvious than the pattern in Figure 4a. In the eastern region, no earthquakes occurred. In the core and west of the Changning anticline, negative anomalies appeared in a large area of positive anomalies.

Figure 5 shows the total intensity gradients of magnetic anomalies in the Changning area. In general, a strong magnetic anomaly gradient indicates that the magnetic source is not evenly distributed [31]. In Figure 5, larger magnetic anomaly gradient variations are located in the northern part of the study area, in the western and northeastern parts of the Changning anticline, and around the Jianwu syncline. There is no correspondence between earthquakes and gradients. Around the Jianwu syncline, the magnetic anomaly gradient distribution is scattered, and the earthquakes are scattered as well. In the Changning anticline, the contour of the large magnetic anomaly gradient area is consistent with the contour of the Changning anticline, the location of which is slightly more southern, by about 2 km. In the Changning anticline, earthquakes mostly occur in a low magnetic anomaly gradient area. In the middle of the anticline, there is a continuous high magnetic anomaly gradient area, which is the earthquake boundary. Earthquakes mainly occur in the west, and no earthquakes occur in the east.

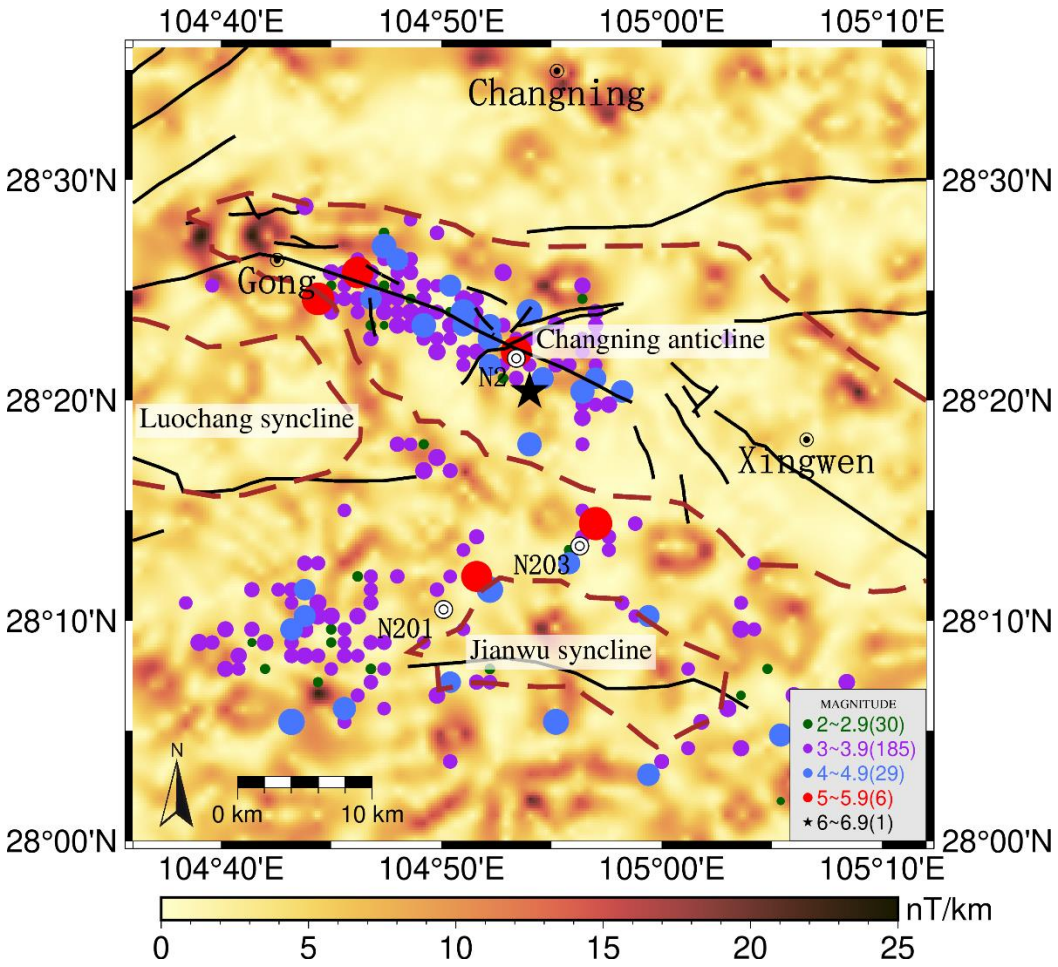

Figure 5. Total intensity gradients of magnetic anomalies in the Changning area.

4.2. Characteristics of Magnetic Basement Depth

The final distribution of the magnetic basement relief was obtained after 50 iterations of the inversion algorithm, as shown in Figure 6. As can be seen, the magnetic basement relief in the Changning area is from 5.3 to 7.2 km (average depth of 6.1 km) in the NW–SE direction, consistent with the magnetic anomalies. The depth in the west of the Changning anticline varies greatly. The northwestern Changning area is interspersed with a shallower area, between the Changning anticline and the Luochang syncline, and the eastern area is relatively flat. The Luochang syncline is generally deeper in the west and shallower in the east. The Jianwu syncline's depth varies greatly—it is deep in the west and east and shallow in the middle. Compared with Figure 3, the magnetic basement's depth is consistent with magnetic anomalies, while positive anomalies correspond to a shallower depth, and negative anomalies correspond to a greater depth.

Figure 6a shows that the earthquakes at the magnetic basement depth are well-distributed, and most of them are located in the magnetic basement. It is speculated that most of the earthquakes in the study area have been caused by the reactivation of basement faults [13]. The RMS error is reduced from 0.23 to 7.08E–4 km.

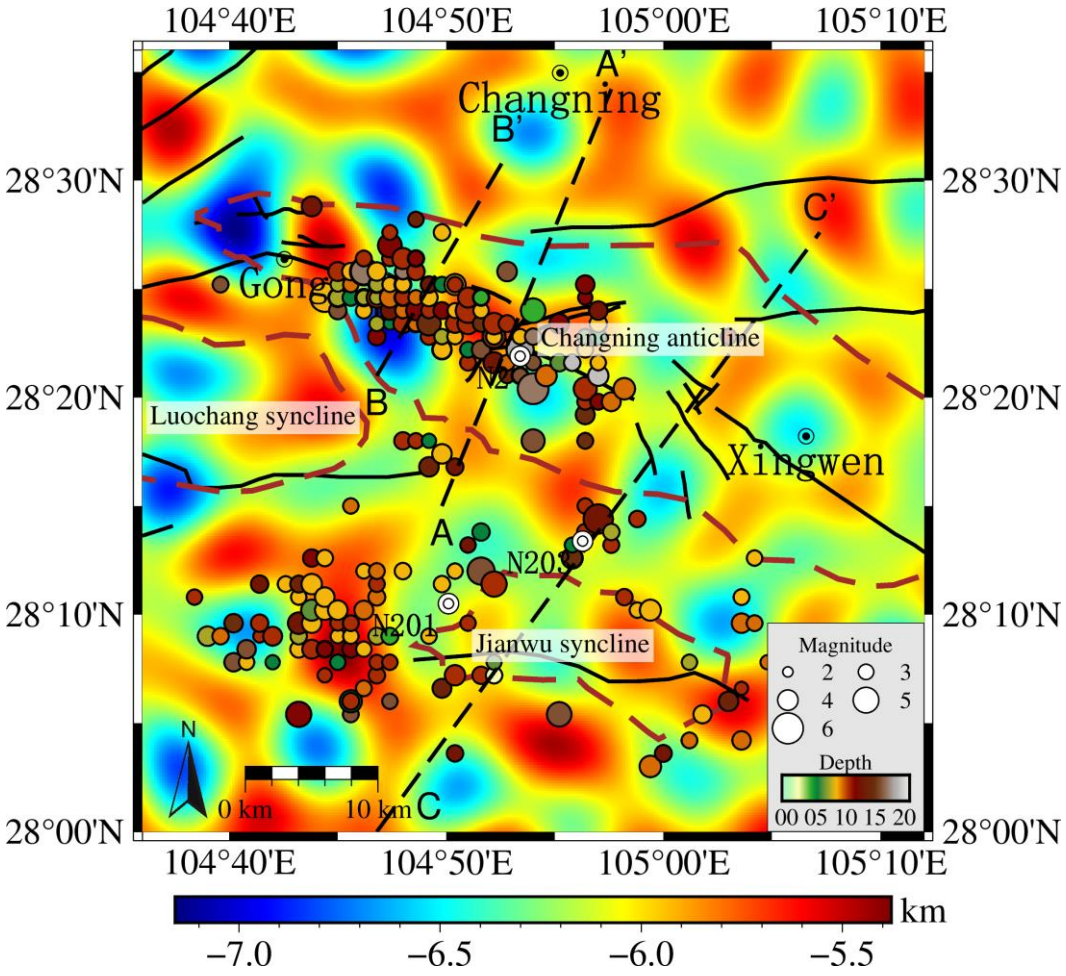

Figure 6. Estimated magnetic basement relief map of the Changning area. The black dotted lines show the location of the three high-resolution seismic reflection profiles from the study by Lu et al. [13]. The magnitudes and depths of earthquakes are shown in the lower right corner.

Five profiles are selected to analyze the magnetic basement depth characteristics in the Changning area, as shown in Figure 7. Profile A-A′ passes through the widest part of the Changning anticline and the western Jianwu syncline in the NE–SW direction. In Figure 7b, the magnetic basement relief is regular, ranging from 5.7 to 6.5 km. Along profile A-A′, there are earthquakes in the A-O segment but no earthquakes in the O-A′ segment. Profile B-B′ traverses the Changning anticline in the NW–W direction. In Figure 7c, the magnetic basement relief changes significantly, ranging from 5.5 to 7.2 km. Along profile B-B′, no earthquakes occurred in the B-P and O-B′ segments, and earthquakes occurred in the P-O section. It can be seen from profile B-B′ that the magnetic basement at the core of the Changning anticline is shallow, which closely corresponds to the geological structure. Profile C-C′ is parallel to A-A′ in the NE–SW direction, passing through the western Changning anticline and the eastern Luochang syncline. In Figure 7d, the magnetic basement changes greatly, ranging from 5.8 to 6.8 km. Earthquakes occurred near point P in the profile, and no earthquakes occurred in the rest of the profile. Profile D-D′ is parallel to A-A′ in the NE–SW direction. The magnetic basement in Figure 7e changes significantly, ranging from 5.6 to 6.7 km. The earthquakes along the profile are concentrated near the Q point and in the western area. Profile E-E′ is parallel to A-A′ in the NE–SW direction, passing through the Changning anticline and the Jianwu syncline. In Figure 7f, the magnetic basement ranges from 5.4 to 6.5 km, and only one earthquake occurred along the profile. In general, most earthquakes occurred in regions with large magnetic basement

gradients, indicating that there are faults or ruptures of geological bodies in this region, which could cause earthquakes.

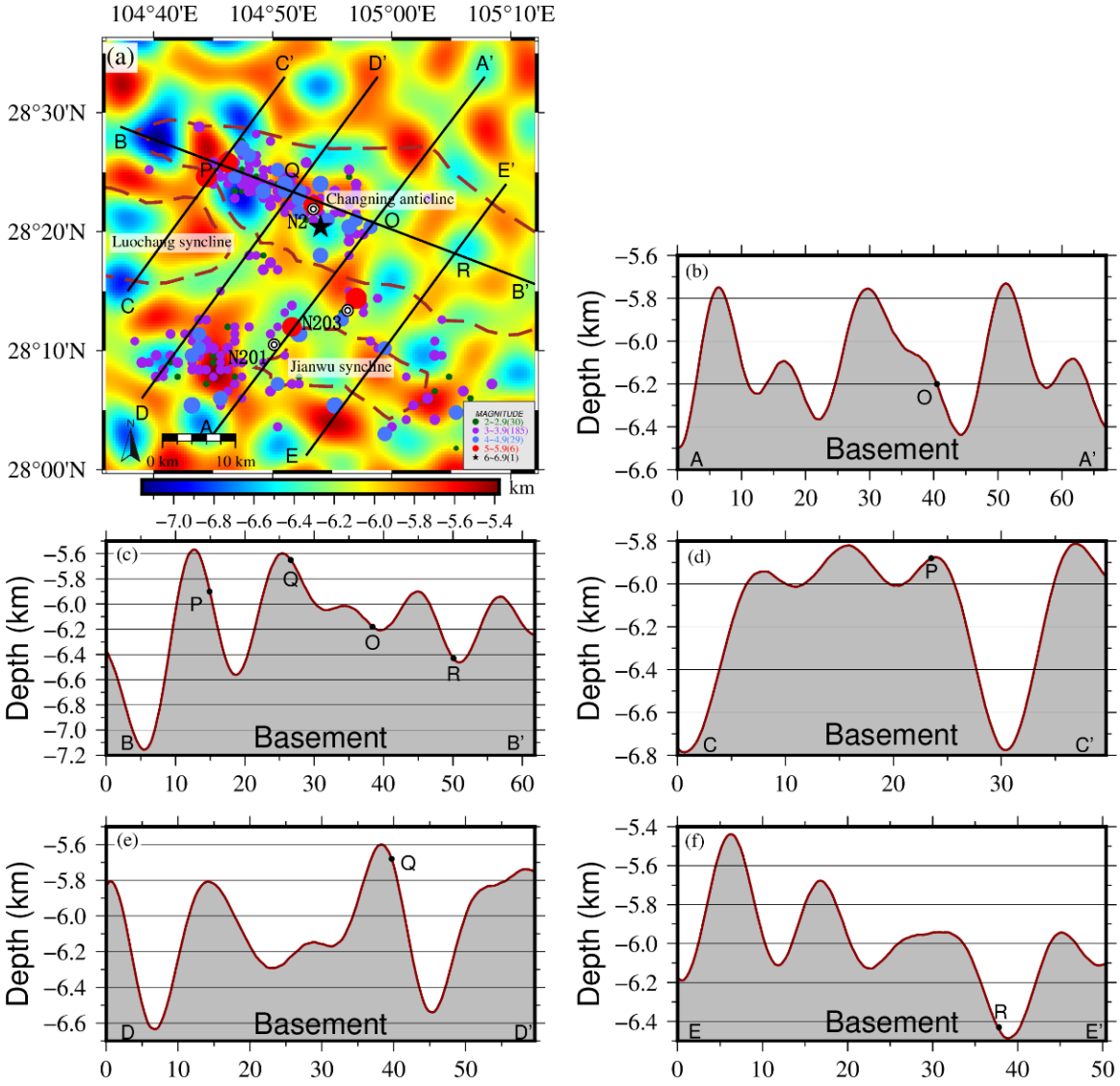

Figure 7. Profiles of magnetic basement relief map in the Changning area. The five black lines are the profiles in (**a**), corresponding to (**b**–**f**), respectively, and the intersection points are O, P, Q and R. The gray area is the magnetic basement in (**b**–**f**).

4.3. Geological Significance of Magnetic Basement

The Sichuan basin basement is mainly composed of magmatic rocks and metamorphic rocks in the middle Neoproterozoic and sedimentary strata of the Nanhua System in the same period. The Sinian Doushantuo Formation and Dengying Formation, and their Upper Phanerozoic strata, serve as the basin caprock, overlying the crystalline basement and Nanhua System unconformity [2,4]. Influenced by the cracking of the Rodinia supercontinent, the Yangtze Craton basement was activated on a large scale, and intense magmatic activity and rifting occurred in the Neoproterozoic period [1,56,57]. High-precision seismic exploration has also revealed obvious rift systems below the Sinian in the Sichuan basin. Most of these rifts are NE, NEE and near-NS, were formed in the late Neoproterozoic, and are closely related to the cracking of the Rodinia supercontinent [43]. Deep well drilling showed that the Nanhua System contained a set of volcanic eruptive rocks or magmatic intrusive rocks with strong magnetism in the Sichuan basin [43]. The distribution map

of the Nanhua rift in the Sichuan basin, compiled from the results of 2D seismic profiles with 5000 km^2 3D seismic data, shows that Neoproterozoic rifts were widely distributed in the basin, mainly with the orientation of NE and N–NE [43]. The Sichuan basin began to subside as a whole after the development of the Nanhua rift, and a set of regional caprocks, the Upper Sinian Dengying Formation, was widely deposited. Affected by the Yangtze Craton's regional extension and the heterogeneity of the Neoproterozoic Nanhua rift basement, the Sinian–Early Cambrian in the Sichuan basin was characterized by the development of large intracratonic rifts and paleo-uplifts, including the NW-trending Dengying Formation II Mianzhu–Changning intracratonic rift [43].

The study of magnetic anomalies is based on differences in rock magnetism. The magnetism of sedimentary caprock can be generally regarded as weak or non-magnetic when compared with the magnetism of the basement and intrusive rock lithologies in which the Precambrian metamorphic basement has undergone fold metamorphism and magma penetration [3,52]. Therefore, magnetic anomalies essentially reflect the Precambrian basement and intrusive rock lithologies [51]. The magnetic basement obtained in this study is relatively complex and is mainly distributed in the northwest direction. Wang et al. studied the basement faults in the Sichuan basin using aeromagnetic data and identified NE- and NW-trending basement faults, including the NW–SE Leshan–Yibin basement fault located in the southwestern basin [58]. Zhou used gravity and magnetic data to identify the extension of the Leshan–Yibin fault, finding that it could exceed 300 km [52].

In summary, as shown in Figure 8, the magnetic basement includes the crystalline basement and the Sinian sedimentary rock metamorphic basement with strong magnetism in the Changning area. High-resolution seismic reflection profiles are sufficiently precise to identify major faults in sedimentary cover. Lu et al. used three high-resolution seismic reflection profiles (shown in Figure 6 and Figures S1–S3 in Supplementary Material S1) to reveal the 3D distributions of the seismogenic faults in the Changning area [13]. In our results, the magnetic basement depth is consistent with the basement depth yielded by seismic reflection profiles, and the basement depth is shallow in the anticline axis. However, the basement depth of seismic profiles is greater than the magnetic basement in this paper, which further indicates that the magnetic basement includes the crystalline basement and part of the Sinian sedimentary metamorphic basement.

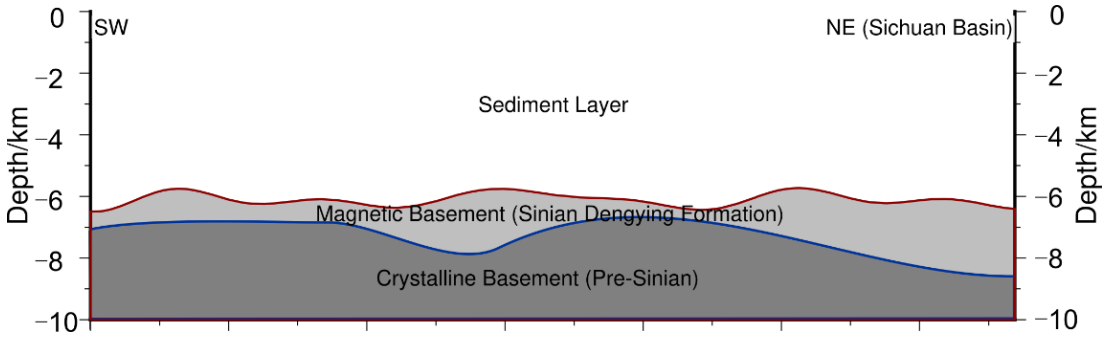

Figure 8. Sketch of magnetic basement structure along the profile AA′ in the Changning area.

To sum up, the origin of magnetic anomalies is related to this large intracratonic rift that developed in the Sinian–Early Cambrian, which plays an important role in the evolution of the Changning area and should also impact magnetic anomalies and the magnetic basement structure.

4.4. Comparison with Other Studies

Hu et al. investigated the seismic wave velocity structure in the Changning area [45]. At a depth of 7 km, we find that the high VP/VS and Poisson's ratio value area corresponds to the deeper magnetic basement, and the low VP/VS and Poisson's ratio value area corresponds to the shallower magnetic basement. In particular, the VP/VS is more

obvious. The VP/VS has three high-value areas, which are located at 104°47′N–28°22′E, 104°42′N–28°09′E and 105°00′N–28°27′E and which correspond to the deeper magnetic basement (see Figure S5 in Supplementary Material S1). The same conclusion applies to the research of Sun et al., who identified the three-dimensional seismic velocity structure of the 17 June 2019 Changning M_S6.0 earthquake [46]. There are differences in the velocity structure because of the differences between the selected stations, recording times, events and processing methods.

The magnetic basement corresponds to the strongly magnetized Pre-Sinian crystalline basement, which is covered by a weakly magnetized sediment, the average lithological density of which is lower than that of the crystalline basement [24,43,52]. This explains why the deeper magnetic basement corresponds to a higher seismic wave velocity ratio. The deeper magnetic basement at the Sinian or Cambrian strata corresponds to a lower lithology density, which corresponds to a higher wave velocity ratio. The mechanical properties of rocks with a high wave velocity ratio are weak; thus, the rock is prone to rupture, which will cause earthquakes [59]. Combined with Figures 4 and 6, the negative magnetic anomaly area corresponds to the deeper magnetic basement, meaning that earthquakes mostly occur in the negative magnetic anomaly area. From the variation in the magnetic basement depth on the Changning anticline axis, it can be inferred that the magnetic basement depth may be the reason for the absence of earthquakes on the western and eastern sides of the anticline.

The northern areas of the three seismic profiles of Lu et al. are all about 2–4 km deeper than the magnetic basement in this article (see Figures S1–S3 in Supplementary Material S1) [13]. Combined with the Sichuan basin's topographic map, we see that the northeastern part is inside the Sichuan basin, while the southwestern part is outside of it. It is inferred from Section 4.3 that the basement in the Sichuan basin is thicker, as are the Sinian sedimentary metamorphic rocks. In addition, previous studies have shown that compared with the entire Sichuan basin, the study area was characterized by weak magnetic anomalies [3,18,29,30]. The average heat flow in the Sichuan basin was 53.7 ± 8.6 mW/m^2, but the average heat flow in the study area was relatively high, at about 60 mW/m^2 [60]. Xiong et al. gave a Curie depth of about 30–40 km in the Sichuan basin based on the aeromagnetic data, while the Curie depth in the study area was about 32 km, which is lower than the average value in the Sichuan basin [30]. Li and Wang used the EMAG2 model to determine that the Curie depth of the study area was about 32 km [61]. Sun et al. developed a three-dimensional model of the lithospheric thermal structure, using the measurements of surface heat production, to give a Curie depth in the study area of about 28 km, which assumes that the Curie isothermal surface temperature was 580 °C [62]. To sum up, the geological structure of the Changning area is complex and special when compared with the rest of the Sichuan basin. From the magnetic anomaly characteristics and magnetic basement structure in the northeastern Changning area, it can be inferred that there is a potential earthquake risk in this area.

5. Conclusions

To systematically study the magnetic characteristics in the Changning area, a magnetic anomaly model was obtained after correcting the diurnal variation and RTP, and the subsurface magnetic basement structure was obtained via an iterative algorithm in the Fourier domain. By comparing the results with those of other studies, the major conclusions reached are as follows:

1. The Changning area magnetic anomaly model, with a resolution of 2 km, indicates a significant difference between the northern salt mine area and the southern shale gas area. Magnetic anomalies in the Changning anticline show continuity, while they are distributed in a more scattered, point-like manner in the Jianwu syncline. The distribution of earthquakes in these two areas also corresponds to the characteristics of magnetic anomalies—earthquakes in the northern part of the study area are concentrated in the Changning anticline, while earthquakes in the southern Jianwu syncline are scattered.

Earthquakes are mostly distributed in the magnetic anomaly zero-line area; in particular, seven earthquakes above Ms5.0 are all within 2 km of the magnetic anomaly zero-line.

2. The magnetic basement relief in the Changning area is from 5.3 to 7.2 km in the NW–SE direction, consistent with magnetic anomalies. There is a great correspondence between magnetic basement depth and magnetic anomalies, as positive magnetic anomalies correspond to the shallower magnetic basement, and negative magnetic anomalies correspond to the deeper magnetic basement. Moreover, earthquakes mostly occur in high-magnetic basement gradient areas, indicating that there are faults or geological ruptures in this region, which could cause earthquakes.

3. The magnetic basement includes the crystalline basement and the Sinian sedimentary metamorphic basement, which has strong magnetism, in the Changning area. It is speculated that the basement is thicker in the Sichuan basin, and the Sinian sedimentary metamorphic rocks are thicker. The origin of magnetic anomalies is related to the large intracratonic rift that developed in the Sinian–Early Cambrian, which may play an important role in the evolution of the Changning area and which should also impact the magnetic anomalies and magnetic basement structure.

4. This explains why a deeper magnetic basement corresponds to a higher seismic wave velocity ratio. The deeper magnetic basement, at the Sinian or Cambrian strata, corresponds to a lower lithology density, which corresponds to a higher wave velocity ratio. The mechanical properties of rocks with a high wave velocity ratio are weak, and thus, the rock is prone to rupture, which will cause earthquakes. The negative magnetic anomaly area corresponds to the deeper magnetic basement; thus, earthquakes mostly occur in negative magnetic anomaly areas. From the variation in magnetic basement depth on the Changning anticline axis, it can be inferred that the magnetic basement depth may be the reason for the absence of earthquakes on the western and eastern sides of the anticline.

This study provides a reference for the magnetic structure in the Changning area and the subsurface dynamic process in the southern margin of the Sichuan basin. Magnetic basement inversion probably cannot accurately describe the fine subsurface structure in this area, and drilling and seismic profiles are needed to further verify the deep tectonic structure in the Changning area. In addition, focusing on the earthquake gap in the western and eastern Changning anticlines and the Luochang syncline, earthquake risks and the potential for larger earthquakes should be re-evaluated.

Supplementary Materials: The supporting information can be found at https://www.mdpi.com/article/10.3390/rs15010023/s1.

Author Contributions: Conceptualization, C.D.; methodology, B.C.; validation, C.D., B.C. and C.W.; investigation, C.D.; data curation, C.W.; writing—original draft preparation, C.D.; writing—review and editing, C.W.; visualization, C.D.; funding acquisition, C.D. All authors have read and agreed to the published version of the manuscript.

Funding: This research was funded by the National Natural Science Foundation of China (42004049).

Data Availability Statement: Magnetic anomaly data are provided by the China Earthquake Administration and can be downloaded at https://zenodo.org/record/6669231. Earthquake catalogs are from http://www.ceic.ac.cn/history. The IGRF-13 model coefficients are from the National Geophysical Data Center https://www.ngdc.noaa.gov/IAGA/vmod/igrf.html. The EMAG2 model is from http://www.geomag.org/models/emag2.html (accessed on 15 November 2022). Figures were prepared using Generic Mapping Tools [63].

Conflicts of Interest: The authors declare no conflict of interest.

References

1. Dong, S.; Gao, R.; Yin, A.; Guo, T.; Zhang, Y.; Hu, J.; Li, J.; Shi, W.; Li, Q. What drove continued continent-continent convergence after ocean closure? Insights from high-resolution seismic-reflection profiling across the Daba Shan in central China. *Geology* **2013**, *41*, 671–674. [CrossRef]
2. Gao, R.; Chen, C.; Wang, H.; Lu, Z.; Brown, L.; Dong, S.; Feng, S.; Li, W.; Wen, Z.; Li, F. SINOPROBE deep reflection profile reveals a Neo-Proterozoic subduction zone beneath The Sichuan basin. *Earth Planet. Sci. Lett.* **2016**, *454*, 86–91. [CrossRef]

3. Wang, J.; Yao, C.; Li, Z.; Zheng, Y.; Shen, X.; Zeren, Z.; Liu, W. 3D inversion of the Sichuan basin magnetic anomaly in South China and its geological significance. *Earth Planets Space* **2020**, *72*, 40. [CrossRef]
4. Zhang, Z.; Wang, Y.; Chen, Y.; Houseman, G.A.; Tian, X.; Wang, E.; Teng, J. Crustal structure across Longmenshan fault belt from passive source seismic profiling. *Geophys. Res. Lett.* **2009**, *36*, L17310. [CrossRef]
5. Lei, X.; Wang, Z.; Su, J. The December 2018 ML5.7 and January 2019 ML5.3 earthquakes in south Sichuan basin induced by shale gas hydraulic fracturing. *Seismol. Res. Lett.* **2019**, *90*, 1099–1110. [CrossRef]
6. Lei, X.; Su, J.; Wang, Z. Growing seismicity in the Sichuan basin and its associated with industrial activities. *Sci. China Earth Sci.* **2020**, *63*, 1633–1660. [CrossRef]
7. Sheng, M.; Chu, R.; Ni, S.; Wang, Y.; Jiang, L.; Yang, H. Source parameters of three moderate size earthquakes in Weiyuan, China, and their relations to shale gas hydraulic fracturing. *J. Geophys. Res. Solid Earth* **2020**, *125*, e2020JB019932. [CrossRef]
8. Deng, Q.; Zhang, P.; Ran, Y.; Yang, X.; Yan, W.; Chen, L. Active tectonics and earthquake activities in China. *Earth Sci. Front.* **2003**, *10*, 66–73. (In Chinese)
9. Foulger, G.R.; Wilson, M.P.; Gluyas, J.G.; Julian, B.R.; Davies, R.J. Global review of human-induced earthquakes. *Earth-Sci. Rev.* **2018**, *178*, 438–514. [CrossRef]
10. Weingarten, M.; Ge, S.; Godt, J.W.; Bekins, B.A.; Rubinstein, J.L. High-rate injection is associated with the increase in US mid-continent seismicity. *Science* **2015**, *348*, 1336–1340. [CrossRef]
11. Clerc, F.; Harrington, R.M.; Liu, Y.; Gu, Y.J. Stress drop estimates and hypocenter relocations of induced seismicity near Crooked Lake, Alberta. *Geophys. Res. Lett.* **2016**, *43*, 6942–6951. [CrossRef]
12. Van Eck, T.; Goutbeek, F.; Haak, H.; Dost, B. Seismic hazard due to small-magnitude, shallow-source, induced earthquakes in The Netherlands. *Eng. Geol.* **2006**, *87*, 105–121. [CrossRef]
13. Lu, R.; He, D.; Liu, J.Z.; Tao, W.; Huang, H.; Xu, F.; Liu, G. Seismogenic Faults of the Changning Earthquake Sequence Constrained by High-Resolution Seismic Profiles in the Southwestern Sichuan basin, China. *Seismol. Res. Lett.* **2021**, *92*, 3757–3766. [CrossRef]
14. Sun, X.; Yang, P.; Zhang, Z. A study of earthquakes induced by water injection in the Changning salt mine area, SW China. *J. Asian Earth Sci.* **2017**, *136*, 102–109. [CrossRef]
15. Meng, L.; McGarr, A.; Zhou, L.; Zang, Y. An Investigation of Seismicity Induced by Hydraulic Fracturing in the Sichuan basin of China Based on Data from a Temporary Seismic Network An Investigation of Seismicity Induced by Hydraulic Fracturing in the Sichuan basin. *Bull. Seismol. Soc. Am.* **2019**, *109*, 348–357. [CrossRef]
16. Tan, Y.; Hu, J.; Zhang, H.; Chen, Y.; Qian, J.; Wang, Q.; Zha, H.; Tang, P.; Nie, Z. Hydraulic fracturing induced seismicity in the Southern Sichuan basin due to fluid diffusion inferred from seismic and injection data analysis. *Geophys. Res. Lett.* **2020**, *47*, e2019GL084885. [CrossRef]
17. Zhao, M.; Tang, L.; Chen, S.; Su, J.; Zhang, M. Machine learning based automatic foreshock catalog building for the 2019 MS6.0 Changning, Sichuan earthquake. *Chin. J. Geophys.* **2021**, *64*, 54–66. (In Chinese) [CrossRef]
18. Maus, S.; Barckhausen, U.; Berkenbosch, H.; Bournas, N.; Brozena, J.; Childers, V.; Dostaler, F.; Fairhead, J.D.; Finn, C.; von Frese, R.B.; et al. EMAG2: A 2-arc min resolution Earth Magnetic Anomaly Grid compiled from satellite, airborne, and marine magnetic measurements. *Geochem. Geophys. Geosyst.* **2009**, *10*, 1130–1143. [CrossRef]
19. Ou, J.; Du, A.; Thébault, E.; Xu, W.; Tian, X.; Zhang, T. A high resolution lithospheric magnetic field model over China. *Sci. China Earth Sci.* **2013**, *56*, 1759–1768. [CrossRef]
20. Chen, C.H.; Lin, J.Y.; Gao, Y.; Lin, C.H.; Han, P.; Chen, C.R.; Lin, L.; Huang, R.; Liu, J.Y. Magnetic pulsations triggered by microseismic ground motion. *J. Geophys. Res. Solid Earth* **2021**, *126*, e2020JB021416. [CrossRef]
21. Maus, S.; Rother, M.; Hemant, K.; Stolle, C.; Lühr, H.; Kuvshinov, A.; Olsen, N. Earth's lithospheric magnetic field determined to spherical harmonic degree 90 from CHAMP satellite measurements. *Geophys. J. Int.* **2006**, *164*, 319–330. [CrossRef]
22. Ou, J.; Du, A.; Xu, W. Investigation of the SA evolution by using the CHAOS-4 model over 1997–2013. *Sci. China Earth Sci.* **2016**, *59*, 1041–1050. [CrossRef]
23. Yang, T.; Dekkers, M.J.; Chen, J. Thermal alteration of pyrite to pyrrhotite during earthquakes: New evidence of seismic slip in the rock record. *J. Geophys. Res. Solid Earth* **2018**, *123*, 1116–1131. [CrossRef]
24. Yang, T.; Chen, J.; Xu, H.; Dekkers, M.J. High-velocity friction experiments indicate magnetic enhancement and softening of fault gouges during seismic slip. *J. Geophys. Res. Solid Earth* **2019**, *124*, 26–43. [CrossRef]
25. Gao, Y.; Zhao, G.; Chong, J.; Klemperer, S.L.; Han, B.; Jiang, F.; Wen, J.; Chen, X.; Zhang, Y.; Tang, J.; et al. Coseismic electric and magnetic signals observed during 2017 Jiuzhaigou M w 6.5 earthquake and explained by electrokinetics and magnetometer rotation. *Geophys. J. Int.* **2020**, *223*, 1130–1143. [CrossRef]
26. Dong, C.; Chen, B.; Yuan, J.; Wang, Z.; Wang, C. Characteristic analysis of the lithospheric magnetic anomaly before the Madoi M_S7.4 earthquake on 22th May 2021. *Acta Seismol. Sin.* **2021**, *43*, 453–462. (In Chinese) [CrossRef]
27. Hamed, S.; Nabi, A.E. Curie point depth beneath the Barramiya-Red Sea coast area estimated from spectral analysis of aeromagnetic data. *J. Asian Earth Sci.* **2012**, *43*, 254–266.
28. Wen, L.; Kang, G.; Bai, C.; Gao, G. Relationship between crustal magnetic anomalies and strong earthquake activity in the south segment of the China North-South Seismic Belt. *Appl. Geophys.* **2021**, *18*, 408–419. [CrossRef]
29. Gu, Z.; Wang, Z. The discovery of Neoproterozoic extensional structures and its significance for gas exploration in the Central Sichuan Block, The Sichuan basin, South China. *Sci. China Earth Sci.* **2014**, *57*, 2758–2768. [CrossRef]

30. Xiong, S.; Yang, H.; Ding, Y.; Li, Z. Characteristics of Chinese continent Curie point isotherm. *Chin. J. Geophys.* **2016**, *59*, 3604–3617. (In Chinese) [CrossRef]
31. Raymond, C.A.; Blakely, R.J. Crustal magnetic anomalies. *Rev. Geophys.* **1995**, *33*, 177–183. [CrossRef]
32. Li, B.; Song, Y.; Wang, Q.; Wang, Z.; Guo, L.; Jiang, J.; Geng, S.; Deng, M.; Zhou, D. Magnetic field characteristics and geological significance of The Sichuan basin. *Geophys. Geochem. Explor.* **2018**, *42*, 937–945. (In Chinese)
33. Parker, R.L. The rapid calculation of potential anomalies. *Geophys. J. R. Astron. Soc.* **1973**, *31*, 447–455. [CrossRef]
34. Pham, L.T.; Oksum, E.; Gómez-Ortiz, D.; Do, T.D. MagB_inv: A high performance Matlab program for estimating the magnetic basement relief by inverting magnetic anomalies. *Comput. Geosci.* **2020**, *134*, 104347. [CrossRef]
35. Blakely, R.J. *Potential Theory in Gravity and Magnetic Applications*; Cambridge University Press: Cambridge, UK, 1995. [CrossRef]
36. Thompson, D.T. EULDPH: A new technique for making computer-assisted depth estimates from magnetic data. *Geophysics* **1982**, *47*, 31–37. [CrossRef]
37. Reid, A.B.; Allsop, J.M.; Granser, H.; Millett, A.J.; Somerton, I.W. Magnetic interpretation in three dimensions using Euler deconvolution. *Geophysics* **1990**, *55*, 80–91. [CrossRef]
38. Curto, J.B.; Diniz, T.; Vidotti, R.M.; Blakely, R.J.; Fuck, R.A. Optimizing depth estimates from magnetic anomalies using spatial analysis tools. *Comput. Geosci.* **2015**, *84*, 1–9. [CrossRef]
39. Spector, A.; Grant, F.S. Statistical models for interpreting aeromagnetic data. *Geophysics* **1970**, *35*, 293–302. [CrossRef]
40. Bansal, A.R.; Gabriel, G.; Dimri, V.P.; Krawczyk, C.M. Estimation of depth to the bottom of magnetic sources by a modified centroid method for fractal distribution of sources: An application to aeromagnetic data in Germany. *Geophysics* **2011**, *76*, L11–L22. [CrossRef]
41. Ravat, D.; Morgan, P.; Lowry, A.R. Geotherms from the temperature-depth constrained solutions of 1-D steady-state heat flow equation. *Geosphere* **2016**, *12*, 1187–1197. [CrossRef]
42. Kumar, R.; Bansal, A.R.; Ghods, A. Estimation of Depth to Bottom of Magnetic Sources Using Spectral Methods: Application on Iran's Aeromagnetic Data. *J. Geophys. Res. Solid Earth* **2020**, *125*, e2019JB018119. [CrossRef]
43. Wei, G. Structural characteristics and oil and gas in Sichuan Basin. Science Press: Beijing, China, 2019.
44. He, D.; Lu, R.; Huang, H.; Wang, X.; Jiang, H.; Zhang, W. Tectonic and geological setting of the earthquake hazards in the Changning shale gas development zone, The Sichuan basin, SW China. *Pet. Explor. Dev.* **2019**, *46*, 1051–1064. [CrossRef]
45. Hu, X.; Cui, X.; Zhang, G.; Wang, G.; Shi, B.; Jiang, D. Analysis on the mechanical causes of the complex seismicity in Changning area, China. *Chin. J. Geophys.* **2021**, *64*, 1–17. (In Chinese) [CrossRef]
46. Sun, Q.; Pei, S.; Su, J.; Liu, Y.; Xue, X.; Li, J.; Li, L.; Zuo, H. Three-dimensional seismic velocity structure across the 17 June 2019 Changning M_S6.0 earthquake, Sichuan, China. *Chin. J. Geophys.* **2021**, *64*, 36–53. (In Chinese) [CrossRef]
47. Kuang, W.; Bloxham, J. An Earth-like numerical dynamo model. *Nature* **1997**, *389*, 371–374. [CrossRef]
48. Dong, C.; Zhang, H.; Jiao, L.; Cheng, H.; Yuen, D.A.; Shi, Y. The Non-Negligible Effect of Viscosity Diffusion on the Geodynamo Process. *J. Geophys. Res. Solid Earth* **2021**, *126*, e2020JB021281. [CrossRef]
49. Chen, B.; Yuan, J.; Wang, C.; Xu, R.; Wang, Z. Data processing flowchart of Chinese mobile geomagnet monitoring array. *J. Seismol. Res.* **2017**, *40*, 335–339. (In Chinese)
50. Alken, P.; Thébault, E.; Beggan, C.D.; Amit, H.; Aubert, J.; Baerenzung, J.; Bondar, T.N.; Brown, W.J.; Califf, S.; Chambodut, A.; et al. International geomagnetic reference field: The thirteenth generation. *Earth Planets Space* **2021**, *73*, 1–25. [CrossRef]
51. Xiong, S.; Ding, Y.; Li, Z. Characteristics of China continent magnetic basement depth. *Chin. J. Geophys.* **2014**, *57*, 3981–3993. (In Chinese) [CrossRef]
52. Zhou, W. Gravity and Magnetic Anomalies in the Sichuan Basin, China: Implications for Deep Structure. Master's Thesis, Nanjing University, Nanjing, China, 2016. (In Chinese).
53. Johnston, M.J.S.; Sasai, Y.; Egbert, G.D.; Mueller, R.J. Seismomagnetic effects from the long-awaited 28 September 2004 M 6.0 Parkfield earthquake. *Bull. Seismol. Soc. Am.* **2006**, *96*, S206–S220. [CrossRef]
54. Xiong, S.; Yang, H.; Ding, Y.; Li, Z.; Li, W. Distribution of igneous rocks in China revealed by aeromagnetic data. *J. Asian Earth Sci.* **2016**, *129*, 231–242. [CrossRef]
55. Oldenburg, D.W. The inversion and interpretation of gravity anomalies. *Geophysics* **1974**, *39*, 526–536. [CrossRef]
56. Li, Z.X.; Bogdanova, S.; Collins, A.S.; Davidson, A.; De Waele, B.; Ernst, R.E.; Fitzsimons, I.C.W.; Fuck, R.A.; Gladkochub, D.P.; Jacobs, J.; et al. Assembly, configuration, and break-up history of Rodinia: A synthesis. *Precambrian Res.* **2008**, *160*, 179–210. [CrossRef]
57. Zhao, G.; Cawood, P.A. Precambrian geology of China. *Precambrian Res.* **2012**, *222*, 13–54. [CrossRef]
58. Wang, Z.C.; Zhao, W.Z.; Li, Z.Y.; Jiang, X.F.; Jun, L. Role of basement faults in gas accumulation of Xujiahe Formation, Sichuan Basin. *Pet. Explor. Dev.* **2008**, *35*, 541–547. [CrossRef]
59. Zandt, G.; Ammon, C.J. Continental crust composition constrained by measurements of crustal Poisson's ratio. *Nature* **1995**, *374*, 152–154. [CrossRef]
60. Jiang, G.; Hu, S.; Shi, Y.; Zhang, C.; Wang, Z.; Hu, D. Terrestrial heat flow of continental China: Updated dataset and tectonic implications. *Tectonophysics* **2019**, *753*, 36–48. [CrossRef]
61. Li, C.; Wang, J. Variations in Moho and Curie depths and heat flow in Eastern and Southeastern Asia. *Mar. Geophys. Res.* **2016**, *37*, 1–20. [CrossRef]

62. Sun, Y.; Dong, S.; Wang, X.; Liu, M.; Zhang, H.; Shi, Y. Three-dimensional thermal structure of East Asian continental lithosphere. *J. Geophys. Res. Solid Earth* **2022**, *127*, e2021JB023432. [CrossRef]
63. Wessel, P.; Smith, W.H.; Scharroo, R.; Luis, J.; Wobbe, F. Generic mapping tools: Improved version released. *Eos Trans. Am. Geophys. Union* **2013**, *94*, 409–410. [CrossRef]